

Full paper

4D nano-tomography of electrochemical energy devices using lab-based X-ray imaging

T.M.M. Heenan^a, D.P. Finegan^{a,b}, B. Tjaden^a, X. Lu^a, F. Iacoviello^a, J. Millichamp^a, D.J.L. Brett^a, P.R. Shearing^{a,*}^a Electrochemical Innovation Lab, Department of Chemical Engineering, UCL, London WC1E 7JE, U.K^b Transportation and Hydrogen Systems Center, National Renewable Energy Laboratory, 1617, USA Cole Blvd, Lakewood, CO 80401, USA

ARTICLE INFO

Keywords:

Li-ion batteries
 Solid oxide fuel cells
 4D imaging
 X-ray nano tomography
 Degradation

ABSTRACT

Electrochemical energy devices offer a variety of alternate means for low-carbon, multi-scale energy conversion and storage. Reactions in these devices are supported by electrodes with characteristically complex microstructures. To meet the increasing capacity and lifetime demands across a range of applications, it is essential to understand microstructural evolutions at a cell and electrode level which are thought to be critical aspects influencing material and device lifetime and performance. X-ray computed tomography (CT) has become a highly employed method for non-destructive characterisation of such microstructures with high spatial resolution. However, sub-micron resolutions present significant challenges for sample preparation and handling particularly in 4D studies, (three spatial dimensions plus time). Here, microstructural information is collected from the same region of interest within two electrode materials: a solid oxide fuel cell and the positive electrode from a lithium-ion battery. Using a lab-based X-ray instrument, tomograms with sub-micron resolutions were obtained between thermal cycling. The intricate microstructural evolutions captured within these two materials provide model examples of 4D X-ray nano-CT capabilities in tracking challenging degradation mechanisms. This technique is valuable in the advancement of electrochemical research as well as broader applications for materials characterisation.

1. Introduction

Two key technologies for low carbon energy conversion and storage are solid oxide fuel cells (SOFCs) and lithium-ion batteries (Li-ions). SOFCs offer high efficiencies, fuel versatility and the ability to supply hundreds of kilowatts in residential or commercial stationary applications [1], whereas Li-ion batteries are predominantly employed for portable electronics and transport applications due to their high energy and power densities [2].

As both SOFCs and Li-ion batteries are electrochemical devices, they each contain similar components: electrodes and an electrolyte. Both systems also require an electronically insulating membrane separating the anode and cathode to prevent short-circuiting. For the SOFC the electrodes are insulated from one another using a dense ceramic electrolyte, whereas Li-ion cells utilise a polymeric or non-woven separator soaked in liquid electrolyte. Li-ion and SOFC electrodes both contain a

porous microstructure with the addition of electrolyte to maximise reaction site densities whilst maintaining good electronic and ionic conductivities.

SOFCs typically operate above 600 °C which inherently brings high efficiencies through improved kinetics, reducing the need for precious catalysts, but also undesirable degradation due to thermal expansion mismatch between the electrode and electrolyte materials [3–6], particle coarsening [7] and the potential for electrode oxidation [8]. As well as maximising reaction site densities, the addition of electrolyte to the SOFC electrode also combats macroscopic thermal expansion mismatch between constituent cell layers [9], however little can be done to mitigate electrode oxidation if exposed to an oxidising atmosphere. Although operating at much lower temperatures, (<60 °C), the electrode materials within Li-ion batteries can also be exposed to high temperatures (>1000 °C) during abusive electrical and/or thermal operations [10–13].

Abbreviations: CT, Computed tomography; SOFCs, Solid oxide fuel cells; Li-ions, Lithium-ion batteries; REDOX, Reduction and oxidation reactions; FIB, Focused-ion beam; SEM, Scanning electron microscope; ROI, Region of interest; DVC, Digital volume correlation; 2D, Two dimensional; 3D, Three dimensional; 4D, 3D plus time; TPB, Triple-phase boundary; ρ_{TPB} , TPB densities; l_{TPB} , TPB length; τ , Tortuosity factor, Tau; p , Percolation; d_e , Equivalent diameter; V_x , Volumetric composition of material x ; SV_x , Solid volume of material x ; SA_x , Surface area of material x ; SSA_x , Specific surface area of material x ; $SISA_{x,y}$, Specific interfacial surface area of materials x and y

* Corresponding author.

E-mail address: p.shearing@ucl.ac.uk (P.R. Shearing).<https://doi.org/10.1016/j.nanoen.2018.03.001>

Received 21 November 2017; Received in revised form 26 February 2018; Accepted 1 March 2018

Available online 03 March 2018

2211-2855/ © 2018 Published by Elsevier Ltd.

In order for the electrochemical reactions within an *SOFC* to proceed all three phases, pore, metal and ceramic, must be percolated allowing the transport of gases, electrons and ions respectively. The location where these three phases are in contact is widely accepted to be the location of the reaction sites and is named the triple-phase boundary (*TPB*). For the anode, hydrogen (H_2) must be able to travel from the fuel inlet, through the tortuous pore network to the reaction site. Similarly, the water molecules require a percolated path to the cell outlet in order to maintain a desirable reaction stoichiometry. The distribution and connection of the electrode pore network therefore greatly influences the electrochemical performance at diffusion limited currents. The population of the *SOFC* reaction sites and the transport mechanisms in the constituent phases are widely assessed by the characterisation of the *TPB* lengths (l_{TPB}), *TPB* densities (ρ_{TPB}) [14–17], degree of percolation (p) and tortuosity factors (τ) [18–21]. Similar to *SOFCs*, Li-ion batteries require the transport of electrons around an external circuit between the electrodes with ions (Li^+) passing through the electrolyte and electronically insulating membrane. The positive electrode is soaked in liquid electrolyte and consists of a metal oxide ($LiMO_2$) where Li^+ and electrons are released from the reaction site during charging. From here, the ions pass through the electrolyte to the graphitic carbon negative electrode creating a lithium-carbon compound (Li_xC_6).

During fabrication the *SOFC* anode is deposited as a metal-oxide, typically nickel oxide, with the addition of zirconia- or ceria-based ceramic electrolyte particles. The metal-oxide is then reduced to its electrically conducting metallic form during the first operational cycle. So long as the anode remains in a reducing environment, free of impurities, the metal should remain metallic however, *SOFCs* are expected to experience many reduction and oxidation (*REDOX*) cycles throughout the lifetime of the stack due to fuel interruption, sealant damage and excessive fuel utilisation. Each *REDOX* cycle is accompanied by a structural change through the expansion of the metal during transition to metal oxide, along with a reduction in the electrode porosity. This structural cycling has been seen to be irreversible resulting in accumulated strain and cracking over the lifetime of the cell, gaining great interest in the microstructural research of *SOFC* degradation [8,22].

Undesirable temperature elevations can arise within Li-ion batteries during operation as an effect of mechanical damage, abnormal electrical conditions or an external heat source. Once a critical temperature is reached the active materials begin to break down in a cascade of exothermic reactions known as thermal runaway. The specific surface area (*SSA*) of the electrode material determines the rate of reaction and hence the rate of heat generation during thermal runaway. This stems from a large portion of the thermal runaway reactions occurring at the interface between the electrode particles and the liquid electrolyte. In a previous study [23] it was observed that the particle size distribution changes during the thermal runaway process, where particles crack and breakdown, exacerbating the thermal runaway process by increasing the specific surface area of the electrode. However, quantifying this change *in-situ* within the complex high temperature environment is extremely challenging due to the extremely high temporal and spatial resolutions required.

Due to this intimate link between microstructure and electrochemical performance through structural metrics such as the triple-phase boundary and specific surface area, system degradation can be correlated to microstructural evolution *via* four-dimensional (4D) studies, three spatial dimensions plus time. In order to better understand the structural evolutions which lead to, and result from, mechanisms such as thermal shock within the *SOFC* and thermal runaway within the Li-ion battery much work has been done on the characterisation of device microstructures at cell-level. The two popular methods for microstructural characterisation have been focused ion beam scanning electron microscopy (*FIB-SEM*) [15,16,24,25] and X-ray computed tomography (CT) [14,26–28]. *FIB-SEM* relies upon the destructive *FIB*

milling of the sample between the collection of *SEM* images; therefore inherently does not allow the possibility of 4D studies. X-ray CT does not destroy the sample as the 3D structures are created through the combination of many radiograph projections, therefore enabling 4D studies. Applications that involve significant structural changes over a short period of time often require access to specialised synchrotron facilities due to their inherently higher flux and high-speed imaging capabilities [27–32]. In recent years, due to significant advancements in instrument capabilities, lab-based X-ray nano-CT has emerged as a key technique, having the benefit of being able to obtain non-destructive 3D information with increased availability, allowing the collection of long-term 4D studies at resolutions competitive with specialist synchrotron facilities.

Many features which are attributed to electrochemical degradation are difficult to observe due to the length scale at which they occur; nanometre resolutions are often required [33] which in turn often demands a feret diameter in the order of tens of microns [34]. Although this has been overcome by the use of advanced techniques such as *FIB* lift-out, the availability of such techniques can be limited and sometimes present inadequate durability [22]. This has resulted in the use of quick, low-cost alternatives such as fast-set epoxies [14] despite the fact that techniques such as this offer minimal durability in operationally relevant environments, restricting analysis to room-temperature.

Here, we present a 4D tomography technique through the creation of mechanically robust samples which allow repeated tomograms of the same region of interest (*ROI*) collected between exposures to high temperature environments. 3D information was reconstructed from an *SOFC* anode and a Li-ion battery electrode which were exposed to high temperatures using two different methods: infrared (*IR*) laser heating of a nickel-yttria stabilised zirconia ($Ni - YSZ$) anode electrode prepared *via* high-precision milling [35], and furnace heating of a lithium cobalt oxide battery electrode on an aluminium (*Al*) current collector prepared using a scalpel under an optical microscope.

This work reports the collection of multiple tomograms for both samples from the same region of interest between exposures to undesirable, high-temperature environments using sub-micron resolution 4D lab-based X-ray nano-CT. The subtle microstructural evolutions which can occur within these two samples during operation provide model examples of this technique's capabilities, not only proving valuable in the continued analysis of electrochemical device microstructures, but also in the structural analysis within many fields of materials engineering.

2. Materials and methods

In order to collect an X-ray nano-CT tomogram many radiographs are collected during the rotation of the sample which are then combined using back projection reconstruction algorithms to form a 3D data-set. Multiple materials can be examined using X-ray nano-CT due to the difference in the attenuation properties between the constituents, often described by the attenuation length or coefficient [14]; with a known beam energy the difference in greyscale, or contrast, between materials can be predicted for the 3D reconstruction. This work utilises a lab-based X-ray nano-CT instrument (Zeiss Xradia 810 Ultra, Carl Zeiss, Pleasanton, CA, U.S.A.) whereby X-rays are generated from a Cr source producing a quasi-monochromatic X-ray beam with a Cr characteristic emission peak of 5.4 keV. A capillary condenser produces focused X-rays for a full-field illumination of the sample which is projected onto the scintillator detector using a Fresnel zone plate, resulting in a square field of view (*FOV*) of $64 \times 64 \mu m$ with accompanying pixel size of 126 nm, when applying a binning of 2. Further detail on the CT system used here can be found elsewhere [36].

The quality of the reconstructed data can be controlled through the optimisation of the signal-to-noise ratio which is dependent upon several factors including: the number of projections, sample thickness and X-ray transmission. Moreover, the statistical representation of the data

is maximised by utilising the entire *FOV* resulting in the largest possible volume to be analysed while maintaining the desired resolution. Thus the optimum sample would be cylindrical in shape with a diameter equivalent to the *FOV* of the X-ray beam although achieving such samples requires high precision instruments [35,37]. Therefore, two preparation techniques were used to demonstrate that high precision methods are advised to maximise *FOV* utilisation and signal-to-noise, particularly for highly attenuating materials such as that which are found in SOFCs, however, it is possible to prepare weakly attenuating samples using a sharp blade under an optical microscope if required.

The following sample-mounting procedure is applicable to the full range of X-ray CT techniques from nanometre to sub-millimetre resolutions. The mounting is resilient to moisture, stable to temperatures above 700 °C, as well as both oxidising and reducing environments, and also contains non-flammable materials with no volatile organic compounds. To produce these samples a primary base coating of high-temperature cement (Aremco Products, New York, U.S.A.) was firstly applied to the tip of an alumina, Al_2O_3 , tube *ca.* 3mm diameter (Multi-lab, England, U.K.). This primary layer was then dried in air at room temperature for 3 h. For the most aggressive conditions it is recommended that the primary layer is cured at 200 °C for 3 h in air ramped at a low rate, *ca.* 1 °C. *min*⁻¹. Once set, the primary surface was coated in a secondary layer with the electrode sample immediately mounted on top of this before drying took place. This should again be dried in air at room temperature for 3 h. If required, the sample can then be refined to a suitable diameter *via* techniques such as high-precision laser lathing [35] or *FIB* milling [37].

Fig. 1 illustrates the mounting procedure demonstrated in this work including a photograph of a prepared sample ready for thermal treatment (Fig. 1.a). The versatility of this technique was extended by the use of hollow alumina tubes during the mounting procedure; hollow tubes allow for a disposable metal pin to be attached to the base of the alumina tube, securing into a sample-holding chuck (Fig. 1.b – d). Utilising disposable pins, specific to the end-station in use, allows for the samples to be entered into any CT instrument or synchrotron beamline independent of the mounting stage dimensions.

Two electrochemical material samples were examined *via* lab-based X-ray nano-CT in this work to demonstrate the high-resolution microstructural information which can be obtained from repeated tomographic analysis on the same *ROI*. The X-ray nano-CT imaging conditions are summarised in Table 1, and the thermal treatment conditions can be found in Table 2. All tomograms were collected at room temperature with use of a lab-based X-ray nano-CT instrument (Zeiss Xradia 810 Ultra, Carl Zeiss, Pleasanton, CA, U.S.A.). Fig. 1.e displays a 3 × 3

Table 1

X-ray nano-CT Imaging parameters for the large *FOV* tomogram collections using the lab-based 4D X-ray nano-CT system for Li-ion and SOFC samples.

	Lithium Ion Battery	Solid Oxide Fuel Cell
Tomograms	<i>Li_000</i> <i>Li_200</i> <i>Li_400</i>	<i>FC_000</i> <i>FC_600</i> <i>FC_750</i> <i>FC_350</i>
Pixel Size (nm)	126	126
Projections	2001	1101
Exposure Time (s)	20	60

mosaic and a single radiograph image of a sample with square 192 μm and 64 μm respective *FOVs*.

The first sample was removed from an SOFC anode (Fuel Cell Materials, OH, U.S.A.); a nickel oxide – yttria-stabilised zirconia, $NiO-(Y_2O_3)_{0.08}(ZrO_2)_{0.92}$, cermet electrode sample was removed from an anode supported cell using an A Series/Compact Class 4 532 nm Laser Micromachining System (Oxford Lasers, Oxford, UK), secured using the cement-mounting technique described above then further machined to the desired diameter for large *FOV* nano-CT (a square 64 × 64 μm *FOV*), the laser milling technique is discussed thoroughly elsewhere [35]. Once machined, the sample was inserted into the X-ray nano-CT instrument and the first tomogram was collected of the untreated sample, *FC_000*. The sample was then exposed to a reduction cycle in a tubular furnace where the temperature was monitored using N-type thermocouples; the nickel oxide–yttria-stabilised zirconia (*NiO* – 8YSZ) sample was thermally ramped at 5 °C. *min*⁻¹ in N_2 to 600°C where it was held in a forming gas (4% H_2 in N_2) atmosphere for 30 mins before being allowed to cool *via* natural convection while maintaining a forming gas environment (see Fig. 2a. – dashed). Reduction was confirmed using Raman spectroscopy; the peaks attributed to NiO at approx. 1070 *cm*⁻¹ were replaced by fluorescence after reduction. As soon as the sample cooled to room temperature, the sample was reinserted into the X-ray nano-CT instrument and the second tomogram was collected of the reduced sample, *FC_600*. The *Ni* – 8YSZ sample was then thermally cycled at a high ramp-rate of 20 °C. *min*⁻¹ to a temperature typical of SOFC operation, 750 °C. Once operating temperature was reached the temperature was not dwelled and the sample was allowed to cool to room temperature *via* natural convection, the entire thermal cycle was conducted within a tubular furnace with a forming gas environment (see Fig. 2a. – solid). After being removed from the tubular furnace the sample was again loaded into an X-ray sample holder (see Fig. 1c.) and the third tomogram was collected, *FC_750*. The sample and chuck were

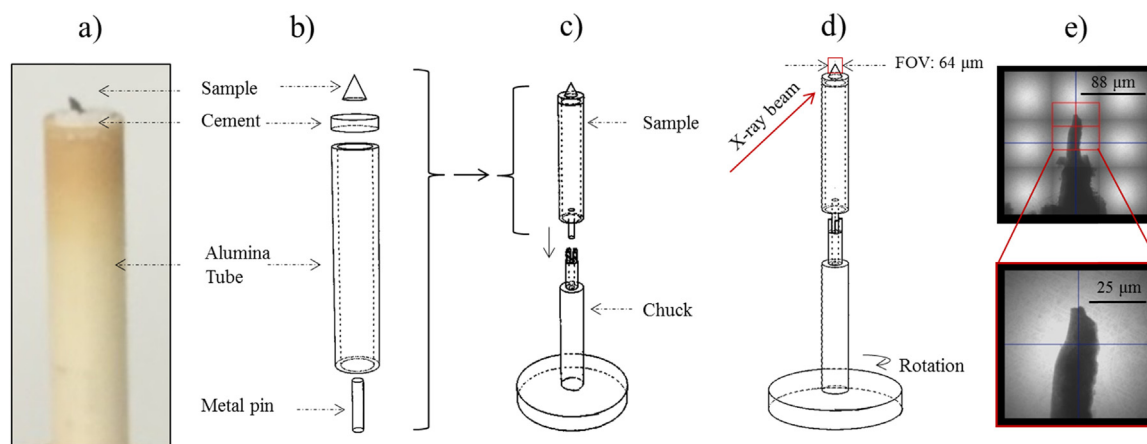


Fig. 1. Procedural diagrams for the preparation of the robust cement-mounting technique utilised for high resolution 4D X-ray nano-CT imaging of thermally induced microstructural evolution: a) mounted sample photographed post-curing, b) schematic diagram of the constituent materials and their location in the mounting assembly, c) schematic diagram of the sample insertion into the sample mounting chuck, d) the orientation of the X-ray nano-CT beam for a lab-based instrument, with e) accompanying 3 × 3 mosaic and single radiograph images with square 192 μm and 64 μm *FOVs*, respectively.

Table 2

Thermal treatment parameters for the tomograms collected pre- and post-thermal cycling of the Li-ion and SOFC samples.

Tomogram	Material(s)	Pretreatment	Heating Method
Li_000	LiCoO ₂ /Al	Untreated	N/A
Li_200	LiCoO ₂ /Al	Cycled to 200°C at 20 °C. min ⁻¹ ; cooled via natural convection in air.	Furnace
Li_400	LiCoO ₂ /Al	Cycled to 400°C at 20 °C. min ⁻¹ in air; cooled via natural convection in air.	Furnace
FC_000	NiO–8YSZ	Untreated	N/A
FC_600	Ni–8YSZ	Ramped to 600°C at 5 °C. min ⁻¹ in N ₂ ; held at 600°C for 30mins in forming gas (4% H ₂ in N ₂); cooled via natural convection in forming gas (4% H ₂ in N ₂).	Furnace
FC_750	Ni–8YSZ	Cycled to 750°C at 20 °C. min ⁻¹ ; cooled via natural convection; ramped and cooled in forming gas (4% H ₂ in N ₂).	Furnace
FC_350	NiO–8YSZ	Cycled to 350°C at 10 °C. min ⁻¹ ; cooled via natural convection in air.	IR Laser

then removed from the X-ray nano-CT instrument to be loaded into a laser heating chamber. Once calibration was complete, the chuck was positioned so that the sample was aligned at the focus point of the High Performance Diode Class 4 980 – 999 nm laser (LIMO Lissotschenko Mikrooptik GmbH, Dortmund, Germany) and subsequently heated in air by increasing the laser power from 0 – 3 W resulting in a ramp rate of 10 °C. min⁻¹ with a peak temperature of ca. 350°C. Once 3W was reached the power was held for a dwell time of 10 min before the laser was switched off and the sample was allowed to cool via natural convection (see Fig. 2a. – spotted). This temperature profile was chosen for two reasons: firstly the authors sought to observe the onset of oxidation; oxidation may be observed from temperatures as low as 200°C [38], but secondly, gasket leakage is a primary cause of anode oxidation [8] and thermal gradients across cells have been observed on the order of hundreds of degrees celcius [4]. Therefore at an operating temperature of 750°C, it is conceivable that a temperature as low as 350°C may be observed at the seal between the gasket and cell wall. Once cooled, the sample was re-inserted into the X-ray nano-CT instrument and a fourth and final tomogram was collected, FC_350. Radiographs were collected

at exposures of 60 s for 1101 projections for all FC_000, FC_600, FC_750 and FC_350 tomograms.

Although the oxidation mechanisms could be triggered using the tubular furnace with an oxygen-containing composition, laser heating allowed the authors to demonstrate that the sample could be kept in the exact same position within the X-ray chuck before, during and after heating, beneficial in the alignment of datasets during the post-processing. For this reason, only the fourth and fifth SOFC tomograms are compared as exact alignment could be made between the two ROIs, yielding a direct assessment of pre- and post-oxidation microstructures. Moreover, the ROI was chosen away from the sample surfaces avoiding any influence of laser sintering which may have occurred during milling [35]. This was chosen for the SOFC sample rather than the Li-ion sample because the average feature size within the SOFC was known to be smaller, making post-processing alignment more difficult requiring the sample to remain within the chuck during thermal treatment in order to directly compare tomograms. Whereas, the particles within the Li-ion sample were large enough to track single particles between thermal treatments without the need for the sample to remain within the X-ray

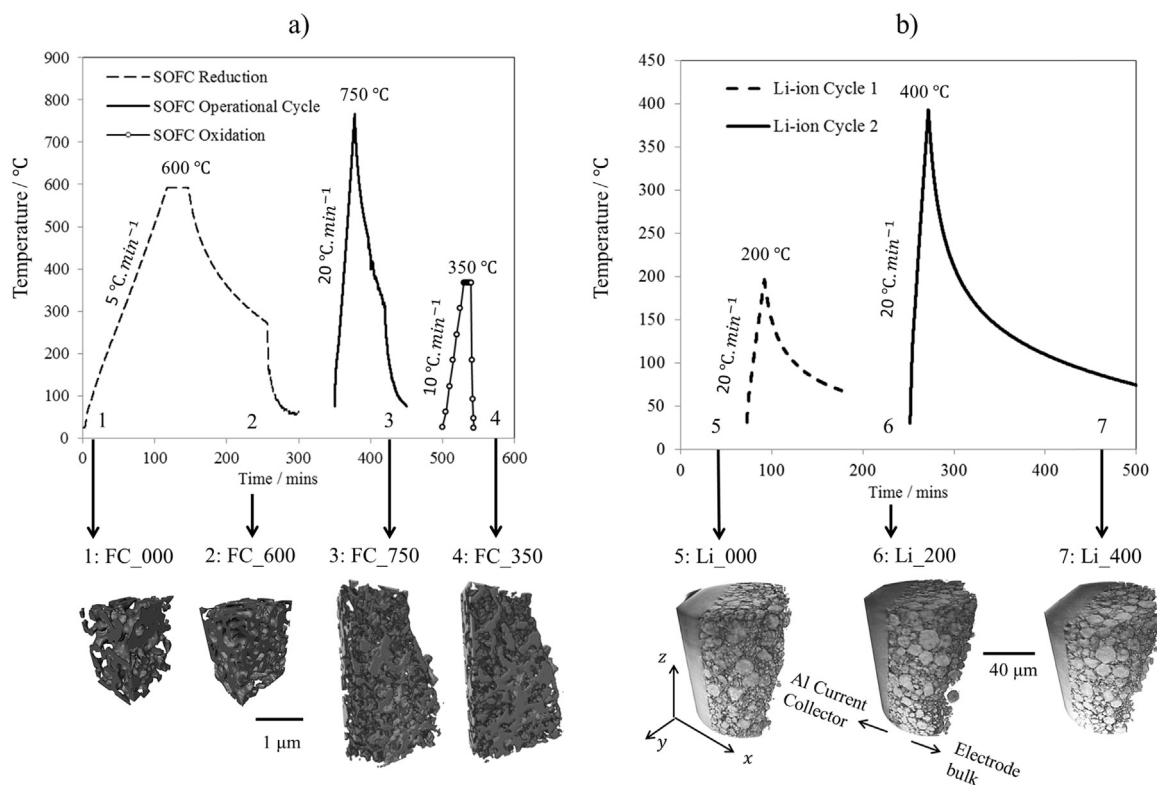


Fig. 2. Temperature profiles for the SOFC and Li-ion samples outlining the thermal treatments which each were exposed to before and after X-ray nano-CT imaging: a) the tubular furnace forming gas atmosphere SOFC reduction and operational thermal cycle, and air atmosphere, laser induced oxidation with tomograms FC_000, FC_600, FC_750 and FC_350 collected at points 1, 2, 3 and 4 respectively, and b) the air atmosphere tubular furnace thermal cycles of the Li-ion sample with sequent tomograms collected at points 5, 6 and 7 for Li_000, Li_200 and Li_400, respectively.

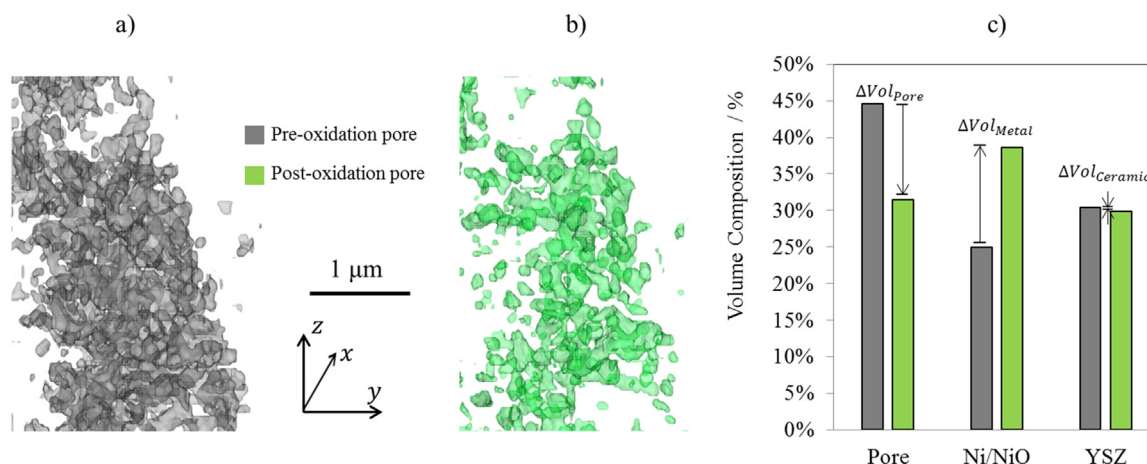


Fig. 3. Oxidation of a Ni – 8YSZ solid oxide fuel cell anode electrode using a laser heating gun: 3D surface renders of the a) *FC_750* grey pre- and b) *FC_350* green post- oxidation pore network, with accompanying volume composition for the three phases: pore, metal (Ni/NiO) and ceramic (YSZ).

chunk.

The second sample was removed from a 160 mAh Li-ion battery (Turnigy, Hong Kong, China); a lithium cobalt oxide, $LiCoO_2$ electrode sample on an aluminium current-collector was prepared using a scalpel under an optical microscope and then secured for imaging using the cement-mounting technique. An internal tomography was taken to ensure that if any structural changes were induced during sample preparation, they were not within the X-ray FOV. Both the electrode and current-collector were captured within the FOV of the X-ray nano-CT machine. Three tomograms were collected from this sample, namely *Li_000*, *Li_200* and *Li_400*. For each tomogram, 2001 projections were collected at an exposure time of 20 s per projection. The first tomogram, *Li_000*, was collected immediately after mounting. The second tomogram, *Li_200*, was collected after cycling the sample within a tubular furnace to 200 °C, and the third tomogram, *Li_400*, was collected after a second thermal cycle to 400 °C. Both thermal cycles were conducted in dry air at a ramp rate of 20 °C. min^{-1} with cooling allowed to occur via natural convection. This temperature profile was chosen to emulate profiles observed during thermal runaway; cell wall temperatures have been detected with thermal imaging to rise to around 200 °C at high ramp rates before plateauing, followed by a rapid temperature increase to excess of 1000 °C after the initiation of thermal runaway [39].

Fig. 2 displays the temperature profiles for the SOFC (Fig. 2.a) and Li-ion (Fig. 2.b) samples with the locations at which each tomography was conducted (noted 1 – 7). Although all profiles were allowed to cool via natural convection after the thermal treatment was complete, there are a few differences in the cooling decay profiles; due to the specific furnace environments used.

After all tomograms were collected the image data was exported as grayscale tagged image format (.tif) stacks and inspected using *Avizo Fire* software (Avizo, Thermo Fisher Scientific, Waltham, Massachusetts, U.S.) and on a *MATLAB* plug-in (Mathworks, Cambridge, U.K.), *Tau Factor* [40]. The effects of microstructural geometry on the transport of gaseous species within heterogeneous structures can be examined with the use of the *MATLAB* application, *Tau Factor* whereby τ is a metric representative of the reduction in diffusive transport caused by convolution in geometry. Using the *Avizo* software all tomograms were filtered using a non-local means filter to enhance image clarity, improving the post-processing alignment of the datasets [41]. The SOFC datasets were also segmented using *Avizo Fire* software into three phases: metal, ceramic and pore, through a cropping of the 3D greyscale histogram [14]. The compositions of the pre- and post-thermal cycling structures were compared by a percentage volume composition (V_x) computed by the summation of all voxels containing each phase in turn. The compositions of the pre- and post-thermal cycling structures were also compared with respect to the percentage of

solid volume composition (SV_x) computed by the summation of all solid (metal and ceramic) voxels containing each phase in turn. A comparison of the percolation and tortuosity factor through the pore phase was examined using *Tau Factor*. The Li-ion data sets were binarized using *Avizo Fire* software into solid and pore phases again through cropping of the 3D greyscale histogram. Once binarized, the particles were separated in order to calculate particle size distributions. The particle size distribution was produced via the calculation of an equivalent diameter (d_e) for each particle within the electrode (i.e. excluding the current collector) [42]. The pore-phase percolation and tortuosity factor values were then assessed using *Tau Factor*.

3. Results and discussion

3.1. Case study 1: oxidation of a solid oxide fuel cell electrode

The influence of heating a Ni – 8YSZ SOFC anode electrode in an oxidising environment was examined by use of 4D X-ray nano-CT. Firstly, by means of qualitative inspection, although the structure and distribution of the pore-phase network pre- and post-heating displayed respectively in Fig. 3.a and Fig. 3.b remains similar, a significant reduction in the total pore-phase volume fraction was observed after the thermal cycle. The extent of the porosity reduction was quantified and is presented in Fig. 3.c and also tabulated in Table 3. As expected, the volume content of the 8YSZ ceramic showed negligible change after the thermal cycle: – 0.51 %. However, Ni metal is known to oxidise from as low as 200 °C, [38] and, given the lack of a reducing agent in the local environment and the presence of the heating laser, the Ni would be expected to oxidise to NiO.

Although the extent of the Ni oxidation would depend on many

Table 3

Volumetric compositional data quantified using lab-based X-ray nano-CT from a Ni – 8YSZ SOFC anode electrode which was examined pre- and post-thermal cycling in an oxidative atmosphere to 350°C using a laser heating gun.

	Pre-oxidation	Post-oxidation	Difference	
			Observed	Expected [8]
Data-set	<i>FC_750</i>	<i>FC_350</i>	N/A	N/A
Sub-volume Analysed (μm^3)	775.83	775.83	0.00	N/A
V_{Pore} (Vol.%)	44.56	31.48	–13.08	–16.56
V_{Metal} (Vol.%)	25.03	38.62	13.59	16.56
$V_{Ceramic}$ (Vol.%)	30.41	29.89	–0.51	0.00
SV_{Metal} (Vol.%)	45.15	56.37	11.22	13.00

factors including the local oxygen partial pressure, microstructure, temperature, volume of Ni, etc., the alteration in the pore-phase volume, metal-phase volume and pore-metal specific interfacial surface area (SISA) can give an indication into the amount of Ni which has been oxidised to NiO. A volumetric increase of 13.59 vol. % was observed in the metal-phase after thermal cycling, resulting in a volumetric reduction of 13.08 vol. % in the pore-phase. For an initial metal solid-volume (the volume only occupied by solid materials, i.e. Ni and YSZ), SV_{Metal} , of 45.15 % the solid volume composition would be expected to increase ca. 13% after complete oxidation. Moreover, an initial porosity of 44.56 % would be expected to reduce to ca. 28 % if fully oxidised [8]. Hence, both the change in metal-phase solid volume composition and the porosity observed here are close to what would be expected from previously presented literature but suggest the sample was not entirely oxidised during this cycle.

The alteration in the electrode composition can result in an unfavourable reduction in the triple-phase boundary density, moreover, if oxidised the electrical conductivity of the metal can be expected to reduce by orders of magnitude [43,44]; resulting in not only a lower volumetric density of electrochemically active reaction sites but also greater Ohmic resistance in the electronic transport and a loss of catalytic activity.

It is observed that the pore-phase tortuosity factor increased substantially after the thermal cycle, likely due to the metal-phase oxidising and obstructing, what were previously well connected pore networks. Although more tortuous, the pore network retained ca. 61% percolation in the x-plane. A tabulated summary of the microstructural information can be found in Table 4.

Although the mechanisms for metal-oxide film growth are complex [38,45], an indication of the film thickness can be obtained by assuming the NiO film grows uniformly into the pore-phase from the metal-pore interface. The specific interfacial surface area of the metal-pore interface prior to thermal cycling is $838 \mu\text{m}^2$, which is ca. 40 % of the total metal surface. Consequently, for a metal-phase volume increase of $106 \mu\text{m}^3$ there would be a ca. 125 nm average film thickness as a result of the oxidation; on average, the metal oxide film grew by one pixel on the metal surface after oxidation. While film thickness is below {C}100 nm, growth can be expected to proceed via logarithmic kinetics following a Mott-Carbrera mechanism whereby ions migrate through the oxide, driven by an electric field, however films thicker than 100 nm can be described by parabolic growth [8]. The kinetics of this temperature profile would predict a film thickness of ca. 190 nm, although the parabolic rate constant is proportional to the local partial pressure of oxygen to the power of a sixth [38]. Given the increasingly tortuous

pore network during oxidation the local partial pressure is likely to be affected, limiting kinetics, thus restricting film growth. An average film thickness of 125 nm is therefore acceptable for this temperature profile and is comparable to previous work studying NiO film growth within SOFC electrodes [22].

3.2. Case study 2: thermal cycling of a Li-ion battery electrode

The thermally induced degradation within a LiCoO₂ battery electrode was investigated via the reconstruction of the three tomograms: Li_000, Li_200 and Li_400, the 3D surface renders for which can be found in Fig. 4.a, Fig. 4.b and Fig. 4.c, respectively.

On inspection of the electrode microstructure it is seen that there was a reduction in the population of the smallest particles and an overall smoothing of the particle surfaces. Thermally-triggered smoothing through aggregation and/or agglomeration of electrode microstructures is a known source of electrochemical degradation, not limited to batteries but also fuel cells [46,47]. A particle size distribution was calculated to accompany each of the surface renders; to do this an equivalent diameter (d_e) for a spherical particle of the same volume was calculated for each of the detectable particles. Each particle was then rounded to the nearest micrometre and all particles with the same equivalent diameter were summated and finally presented as a percentage of the total number of detectable particles. The particle size distributions for the three tomograms: Li_000, Li_200 and Li_400, are presented in Fig. 4.d, Fig. 4.e and Fig. 4.f, respectively.

The quantitative particle size analysis confirmed that after each thermal-cycle there was a reduction in the number of the smallest detectable particles, with diameters smaller than ca. 4 μm , and a growth in the number of larger particles, with diameters greater than ca. 10 μm . An increase in particle size would result in a reduction in available reaction sites due to a reduction in specific surface area, thus leading to a reduction in the cell's rate capabilities. The quantitative analysis was extended to the inspection of the tortuosity factor and specific surface area, presented in Table 5.

Minor variation is seen in the pore-phase tortuosity factor which remains stable averaging a value of 2.1 and deviating ca. 10%. Stable tortuosity factor values suggests that, through temperature effects alone agglomeration and aggregation effects dominate, resulting in minimal change in the pore-phase network paths. Although, during thermal runaway it has been seen that cell innards can become significantly displaced, sometimes accumulating at cell vents/walls and even ejecting some or all of the contents from the cell casing entirely [23].

Finally, as expected from the reduction in the number of small, and increase in the number of large particles, the specific surface area decreases sequentially with each thermal cycle, from $1.73 \mu\text{m}^{-1}$, to $1.63 \mu\text{m}^{-1}$ to $1.51 \mu\text{m}^{-1}$. Therefore even at lower temperatures (ca. 200 °C), where the cell may not have failed catastrophically a reduction in specific surface area and hence rate capability as well as reaction rate during thermal runaway can occur [48].

It has been discussed in previous work [49] that after thermal abuse Li-ion electrode particles can be expected to crack, increasing the electrode's specific surface area, further accelerating thermal runaway. To investigate whether the temperature profiles observed here were sufficient to induce particle cracking such as this, a single large particle was tracked throughout the three tomograms, the evolutions of which can be seen in the 2D cropped-greyscale slices displayed in Fig. 5.d, Fig. 5.e. and Fig. 5.f. with reference to their location within the 3D volume displayed in Fig. 5.a, Fig. 5.b. and Fig. 5.c, respectively. From the 3D volume it is difficult to observe the subtle microstructural difference which is outlined in the 2D slices; the particle was initially undamaged but a small crack ca. 300 nm in thickness spanning the length of the particle (ca. 4 μm) appeared after the first thermal cycle and grew to ca. 600 nm in thickness after the second thermal cycle.

Table 4

A tabulated summary of the 4D nano X-ray nano-CT microstructural data quantified from a Ni – 8YSZ SOFC anode electrode which was examined pre- and post-thermal cycling in an oxidative atmosphere using a laser heating gun.

	Pre- oxidation	Post- oxidation	Difference
Data-set	FC_750	FC_350	–
Tau Factor			
P_{Pore} (Vol. %)	91.30	61.60	–29.70
τ_{Pore} (no-units)	5.90	31.60	25.70
Triple- phase boundary			
l_{TPB} (μm)	2995	1715	–1280
ρ_{TPB} (μm^{-2})	3.86	2.21	–1.65
Specific Surface Area			
SAV_{Pore} (μm^{-1})	1.68	0.95	–0.73
SAV_{Metal} (μm^{-1})	2.66	2.85	0.19
$SAV_{Ceramic}$ (μm^{-1})	2.18	2.30	0.12
Specific Interfacial Surface Area			
$SISA_{Pore-Metal}$ (μm^{-1})	1.08	0.75	–0.33
$SISA_{Metal-Ceramic}$ (μm^{-1})	1.58	2.10	0.52
$SISA_{Ceramic-Pore}$ (μm^{-1})	0.60	0.20	–0.40

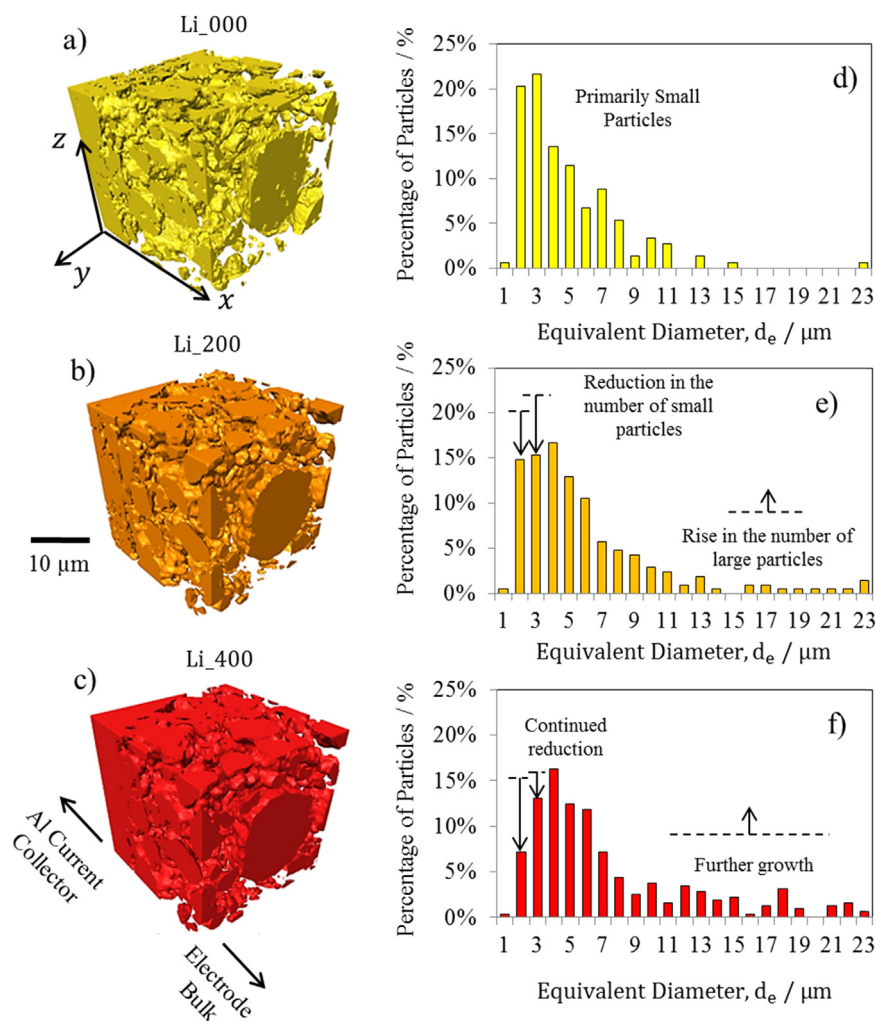


Fig. 4. Thermal cycling of a LiCoO_2/Al Li-ion battery electrode/current-collector sample in an air atmosphere: 3D surface render of the a) fresh, b) after the first cycle to 200 °C, c) after the second cycle to 400 °C, with accompanying particle size distribution for the d) fresh, e) post-cycling to 200 °C and f) post-cycling to 400 °C samples.

Table 5

A tabulated summary of the nano-CT microstructural data quantified from a LiCoO_2/Al Li-ion battery electrode/current-collector sample which was examined pre- and post-thermal cycling in an air atmosphere using tubular furnace.

	Fresh	Post-cycle 1	Post-cycle 2
Data-set	<i>Li_000</i>	<i>Li_200</i>	<i>Li_400</i>
Sub-Volume Analysed (μm^3)	4195	4195	4195
SA (μm^2)	7258	6838	6335
SSA (μm^{-1})	1.73	1.63	1.51
τ_{pore} (no-units)	2.37	1.74	2.20

4. Conclusions

A lab-based 4D X-ray nano-CT technique for the characterisation of thermally driven microstructural changes within *SOFC* and Li-ion battery materials has been demonstrated, microstructural evolutions triggered by thermal abuse were subsequently tracked and quantified.

Within electrochemical devices the phase compositions, reaction site densities, tortuosity factors and specific surface areas are amongst the most significant metrics in correlating structural data to electrochemical performance. The evolution of these metrics results in the degradation, and ultimately the failure of cells. Elevated temperatures are known to trigger such undesirable evolutions although, capturing the variation of these three-dimensional metrics with time is challenging. This technique has been used to inspect two case studies: firstly, to

quantify the decline in porosity and reaction sites, and the increase in pore-phase tortuosity factor during the oxidation of an *SOFC* anode, and secondly, the decrease in particle specific surface area and propagation of cracking within a Li-ion battery electrode due to thermal cycling. Due to the limited availability of X-ray beamlines and the associated high-precision sample preparation instruments, materials statistics have until now been limited. However, through the use of sample preparation techniques such as this and readily accessible lab-based instruments, the authors envisage the creation of large sample libraries which will improve the statistical confidence of materials characterisation.

The application of X-ray nano-CT is not limited to electrochemical devices; X-ray nano-CT has been vastly employed in the study of 3D structures within many materials. Furthermore, the application of image correlation techniques such as digital volume correlation (DVC) and machine learning has enabled further information to be drawn from 4D tomographic studies. The work here demonstrates the first of many studies which will be carried out in the future of lab-based 4D investigations spanning all areas of structural research and subsequent correlative analysis. Moreover, the robust nature of this technique may also be employed for other inspection methods such as X-ray and neutron diffraction, particularly where small sample sizes are required to achieve desired transmissions or extreme conditions are of interest.

Utilising the non-destructive nature of X-ray nano-CT when conducting 4D studies to observe time-dependent mechanisms such as that which are responsible for degradation within electrochemical devices will lead to an improved fundamental understanding of the causes and

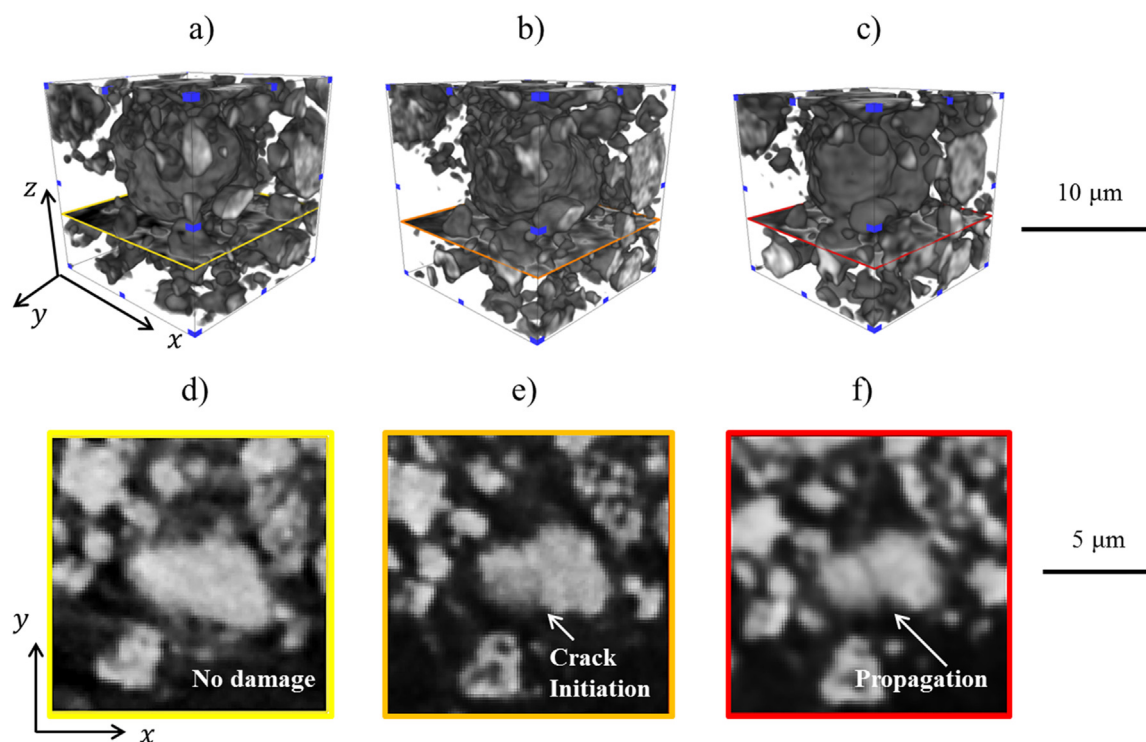


Fig. 5. Tracking the structural evolutions within a single particle from a LiCoO_2/Al Li-ion battery electrode/current-collector sample thermally cycled in an air atmosphere: 3D surface render of a single large particle a) fresh, b) after the first cycle to 200°C, c) after the second cycle to 400°C, with accompanying single 2D slice d) fresh, e) post-cycling to 200°C and f) post-cycling to 400°C showing the development of a crack.

effects which limit electrochemical device performance and lifetime. Such a technique is not limited to the analysis of electrochemical devices but may also be applied in the advancement of broader material characterisation.

Acknowledgements

The authors would like to acknowledge the EPSRC (EP/M014045/1, EP/P009050/1), the Centre for Doctoral training and the Royal Academy for Engineering for financial support, access to the Zeiss Xradia 810 Ultra instrument was supported by the EPSRC (EP/K005030/1).

References

- [1] P.E. Dodds, I. Staffell, A.D. Hawkes, F. Li, P. Grünwald, W. McDowall, P. Ekins, Hydrogen and fuel cell technologies for heating: a review, *Int. J. Hydrog. Energy* 40 (5) (2015) 2065–2083.
- [2] N. Nitta, F. Wu, J.T. Lee, G. Yushin, Li-ion battery materials: present and future, *Mater. Today* 18 (5) (2015) 252–264.
- [3] R. Clague, P.R. Shearing, P.D. Lee, Z. Zhang, D.J.L. Brett, A.J. Marquis, N.P. Brandon, Stress analysis of solid oxide fuel cell anode microstructure reconstructed from focused ion beam tomography, *J. Power Sources* 196 (21) (2011) 9018–9021.
- [4] J.B. Robinson, L.D. Brown, R. Jervis, O.O. Taiwo, T.M. Heenan, J. Millichamp, T.J. Mason, T.P. Neville, R. Clague, D.S. Eastwood, C. Reinhard, Investigating the effect of thermal gradients on stress in solid oxide fuel cell anodes using combined synchrotron radiation and thermal imaging, *J. Power Sources* 288 (2015) 473–481.
- [5] S. Celik, B. Ibrahimoglu, S. Toros, M.D. Mat, Three dimensional stress analysis of solid oxide fuel cell anode micro structure, *Int. J. Hydrog. Energy* 39 (33) (2014) 19119–19131.
- [6] M. Mori, T. Yamamoto, H. Itoh, H. Inaba, H. Tagawa, Thermal expansion of nickel-zirconia anodes in solid oxide fuel cells during fabrication and operation, *J. Electrochem. Soc.* 145 (4) (1998) 1374–1381.
- [7] P. Tanasini, M. Cannarozzo, P. Costamagna, A. Faes, J. Van Herle, A. Hessler-Wyser, C. Comminellis, Experimental and theoretical investigation of degradation mechanisms by particle coarsening in SOFC electrodes, *Fuel Cells* 9 (5) (2009) 740–752.
- [8] D. Sarantaridis, A. Atkinson, REDOX cycling of Ni-based solid oxide fuel cell anodes: a review, *Fuel Cells* 7 (3) (2007) 246–258.
- [9] X. Lu, B. Tjaden, A. Bertei, T. Li, K. Li, D. Brett, P. Shearing, 3D characterization of diffusivities and its impact on mass flux and concentration overpotential in SOFC anode, *J. Electrochem. Soc.* 164 (4) (2017) F188–F195.
- [10] J. Xu, C. Lan, Y. Qiao, Y. Ma, Prevent thermal runaway of lithium-ion batteries with minichannel cooling, *Appl. Therm. Eng.* 110 (2017) 883–890.
- [11] Krishna Shah, Divya Chalise, Ankur Jain, Experimental and theoretical analysis of a method to predict thermal runaway in Li-ion cells, *J. Power Sources* 330 (2016) 167–174.
- [12] S. Yayathi, W. Walker, D. Doughty, H. Ardebili, Energy distributions exhibited during thermal runaway of commercial lithium ion batteries used for human spaceflight applications, *J. Power Sources* 329 (2016) 197–206.
- [13] X. Feng, L. Lu, M. Ouyang, J. Li, X. He, A 3D thermal runaway propagation model for a large format lithium ion battery module, *Energy* 115 (2016) 194–208.
- [14] T.M.M. Heenan, J.J. Bailey, X. Lu, J.B. Robinson, F. Iacoviello, D.P. Finegan, D.J.L. Brett, P.R. Shearing, Three-phase segmentation of solid oxide fuel cell anode materials using lab based X-ray nano-computed tomography, *Fuel Cells* 17 (1) (2017) 75–82.
- [15] J.R. Wilson, W. Kobsiriphat, R. Mendoza, H.Y. Chen, J.M. Hiller, D.J. Miller, K. Thornton, P.W. Voorhees, S.B. Adler, S.A. Barnett, Three-dimensional reconstruction of a solid-oxide fuel-cell anode, *Nat. Mater.* 5 (7) (2006) 541–544.
- [16] H. Iwai, N. Shikazono, T. Matsui, H. Teshima, M. Kishimoto, R. Kishida, D. Hayashi, K. Matsuzaki, D. Kanno, M. Saito, H. Muroyama, Quantification of SOFC anode microstructure based on dual beam FIB-SEM technique, *J. Power Sources* 195 (4) (2010) 955–961.
- [17] X. Lu, T.M. Heenan, J.J. Bailey, T. Li, K. Li, D.J. Brett, P.R. Shearing, Correlation between triple phase boundary and the microstructure of solid oxide fuel cell anodes: the role of composition, porosity and Ni densification, *J. Power Sources* 365 (2017) 210–219.
- [18] X. Lu, T. Li, O.O. Taiwo, J. Bailey, T. Heenan, K. Li, D.J.L. Brett, P.R. Shearing, Study of the tortuosity factors at multi-scale for a novel-structured SOFC anode, *J. Phys.: Conf. Ser.* 849 (1) (2017) 012020 IOP Publishing <https://onlinelibrary.wiley.com/doi/full/10.1111/jmi.12577>.
- [19] B. Tjaden, S.J. Cooper, D.J. Brett, D. Kramer, P.R. Shearing, On the origin and application of the Bruggeman correlation for analysing transport phenomena in electrochemical systems, *Curr. Opin. Chem. Eng.* 12 (2016) 44–51.
- [20] B. Tjaden, D.J. Brett, P.R. Shearing, Tortuosity in electrochemical devices: a review of calculation approaches, *Int. Mater. Rev.* (2016) 1–21.
- [21] R.E. Williford, L.A. Chick, G.D. Maupin, S.P. Simner, J.W. Stevenson, Diffusion limitations in the porous anodes of SOFCs, *J. Electrochem. Soc.* 150 (8) (2003) A1067–A1072.
- [22] P.R. Shearing, R.S. Bradley, J. Gelb, F. Tariq, P.J. Withers, N.P. Brandon, Exploring microstructural changes associated with oxidation in Ni-YSZ SOFC electrodes using high resolution X-ray nano-CT computed tomography, *Solid State Ion.* 216 (2012) 69–72.
- [23] D.P. Finegan, M. Scheel, J.B. Robinson, B. Tjaden, M. Di Michiel, G. Hinds, D.J. Brett, P.R. Shearing, Investigating lithium-ion battery materials during

- overcharge-induced thermal runaway: an operando and multi-scale X-ray nano-CT study, *Phys. Chem. Chem. Phys.* 18 (45) (2016) 30912–30919.
- [24] T. Sui, B. Song, J. Dluhos, L. Lu, A.M. Korsunsky, Nanoscale chemical mapping of Li-ion battery cathode material by FIB-SEM and TOF-SIMS multi-modal microscopy, *Nano Energy* 17 (2015) 254–260.
- [25] S. Vierrath, L. Zielke, R. Moroni, A. Mondon, D.R. Wheeler, R. Zengerle, S. Thiele, Morphology of nanoporous carbon-binder domains in Li-ion batteries—A FIB-SEM study, *Electrochem. Commun.* 60 (2015) 176–179.
- [26] J.R. Izzo, A.S. Joshi, K.N. Grew, W.K. Chiu, A. Tkachuk, S.H. Wang, W. Yun, Nondestructive reconstruction and analysis of SOFC anodes using X-ray computed tomography at sub-50 nm resolution, *J. Electrochem. Soc.* 155 (5) (2008) B504–B508.
- [27] D.P. Finegan, M. Scheel, J.B. Robinson, B. Tjaden, I. Hunt, T.J. Mason, J. Millichamp, M. Di Michiel, G.J. Offer, G. Hinds, D.J. Brett, In-operando high-speed tomography of lithium-ion batteries during thermal runaway, *Nat. Commun.* (2015) 6.
- [28] P.R. Shearing, L.E. Howard, P.S. Jørgensen, N.P. Brandon, S.J. Harris, Characterization of the 3-dimensional microstructure of a graphite negative electrode from a Li-ion battery, *Electrochem. Commun.* 12 (3) (2010) 374–377.
- [29] O.O. Taiwo, J.M. Paz-García, S.A. Hall, T.M. Heenan, D.P. Finegan, R. Mokso, P. Villanueva-Pérez, A. Patera, D.J. Brett, P.R. Shearing, Microstructural degradation of silicon electrodes during lithiation observed via operando X-ray nano-CT tomographic imaging, *J. Power Sources* 342 (2017) 904–912.
- [30] J. Wang, Y.C.K. Chen-Wiegart, J. Wang, In situ three-dimensional synchrotron X-ray nanotomography of the (De) lithiation processes in tin anodes, *Angew. Chem. Int. Ed.* 53 (17) (2014) 4460–4464.
- [31] H. Markötter, I. Manke, P. Krüger, T. Arlt, J. Haussmann, M. Klages, H. Rieseheimer, C. Hartnig, J. Scholta, J. Banhart, Investigation of 3D water transport paths in gas diffusion layers by combined in-situ synchrotron X-ray nano-CT radiography and tomography, *Electrochem. Commun.* 13 (9) (2011) 1001–1004.
- [32] S.M. Ghahari, A.J. Davenport, T. Rayment, T. Suter, J.P. Tinnes, C. Padovani, J.A. Hammans, M. Stapanoni, F. Marone, R. Mokso, In situ synchrotron X-ray nano-CT micro-tomography study of pitting corrosion in stainless steel, *Corros. Sci.* 53 (9) (2011) 2684–2687.
- [33] Y. Guan, W. Li, Y. Gong, G. Liu, X. Zhang, J. Chen, J. Gelb, W. Yun, Y. Xiong, Y. Tian, H. Wang, Analysis of the three-dimensional microstructure of a solid-oxide fuel cell anode using nano X-ray nano-CT tomography, *J. Power Sources* 196 (4) (2011) 1915–1919.
- [34] P.R. Shearing, J. Gelb, N.P. Brandon, X-ray nano-CT nano computerised tomography of SOFC electrodes using a focused ion beam sample-preparation technique, *J. Eur. Ceram. Soc.* 30 (8) (2010) 1809–1814.
- [35] J.J. Bailey, T.M.M. Heenan, D.P. Finegan, X. Lu, S.R. Daemi, F. Iacoviello, N.R. Backeberg, O.O. Taiwo, D.J.L. Brett, A. Atkinson, P.R. Shearing, Laser-preparation of geometrically optimised samples for X-ray nano-CT, *J. Microsc.* 267 (3) (2017) 384–396 <https://onlinelibrary.wiley.com/doi/full/10.1111/jmi.12577>.
- [36] Zeiss Xradia 810 Ultra 'Nanoscale X-ray nano-CT Imaging: Explore at the speed of science' Product information, can be found under http://pages.microscopy.zeiss.com/rs/zeiss/images/EN_42_011_080_Product_810Ultra.pdf.
- [37] P.R. Shearing, J. Golbert, R.J. Chater, N.P. Brandon, 3D reconstruction of SOFC anodes using a focused ion beam lift-out technique, *Chem. Eng. Sci.* 64 (17) (2009) 3928–3933.
- [38] M.J. Graham, M. Cohen, On the mechanism of low-temperature oxidation (23°–450° C) of polycrystalline nickel, *J. Electrochem. Soc.* 119 (7) (1972) 879–882.
- [39] D.P. Finegan, E. Darcy, M. Keyser, B. Tjaden, T.M. Heenan, R. Jervis, J.J. Bailey, R. Malik, N.T. Vo, O.V. Magdysyuk, R. Atwood, Characterising thermal runaway within lithium-ion cells by inducing and monitoring internal short circuits, *Energy Environ. Sci.* 10 (6) (2017) 1377–1388 <http://pubs.rsc.org/-/content/articlehtml/2017/ee/c7ee00385d>.
- [40] S.J. Cooper, A. Bertei, P.R. Shearing, J.A. Kilner, N.P. Brandon, Tau Factor: an open-source application for calculating tortuosity factors from tomographic data, *SoftwareX* 5 (2016) 203–210.
- [41] Antoni Buades, Bartomeu Coll, Jean-Michel Morel, A review of image denoising algorithms, with a new one, *SIAM J. Multiscale Model. Simul.: A SIAM Interdiscip. J.* 4 (2) (2005) 490–530.
- [42] X. Zhang, A.M. Sastry, W. Shyy, Intercalation-induced stress and heat generation within single lithium-ion battery cathode particles, *J. Electrochem. Soc.* 155 (7) (2008) A542–A552.
- [43] M. Yousuf, P.C. Sahu, K.G. Rajan, High-pressure and high-temperature electrical resistivity of ferromagnetic transition metals: nickel and iron, *Phys. Rev. B* 34 (11) (1986) 8086.
- [44] F.J. Morin, Electrical properties of NiO, *Phys. Rev.* 93 (6) (1954) 1199.
- [45] R. Karmhag, G.A. Niklasson, M. Nygren, Oxidation kinetics of nickel nanoparticles, *J. Appl. Phys.* 89 (5) (2001) 3012–3017.
- [46] Y. Shao, G. Yin, Y. Gao, Understanding and approaches for the durability issues of Pt-based catalysts for PEM fuel cell, *J. Power Sources* 171 (2) (2007) 558–566.
- [47] H. Yokokawa, H. Tu, B. Iwanschitz, A. Mai, Fundamental mechanisms limiting solid oxide fuel cell durability, *J. Power Sources* 182 (2) (2008) 400–412.
- [48] F. Röder, S. Sonntag, D. Schröder, U. Krewer, Simulating the impact of particle size distribution on the performance of graphite electrodes in lithium-ion batteries, *Energy Technol.* 4 (12) (2016) 1588–1597.
- [49] Donal P. Finegan, et al., Quantifying bulk electrode strain and material displacement within lithium batteries via high-speed operando tomography and digital volume correlation, *Adv. Sci.* 3 (3) (2016).



Thomas Heenan is a Ph.D. student working in the Electrochemical Innovation Lab at University College London. He completed his Bachelor's Degree in the department of Chemical Engineering in 2014 before joining the E.P.S.R.C. Centre for Doctoral Training (CDT) in Fuel Cells and their fuels. His work is focused on X-ray characterisation of electrochemical devices with a primary focus on mitigating thermally induced degradation in solid oxide fuel cells.



Donal Finegan is a postdoctoral researcher at the US Department of Energy, National Renewable Energy Laboratory. He received his PhD from University College London (UCL) in 2016 where his research focused on the use of X-ray imaging as a diagnostic tool for Li-ion batteries. His current research involves characterisation of materials used in electrochemical energy devices, as well as abuse testing and improving the safety of Li-ion batteries. His work on battery safety is in conjunction with the NASA Johnson Space Centre where safety considerations are implemented and tested on the system scale.



Bernhard Tjaden is a development engineer with the Elingklinger AG. He received his PhD from University College London (UCL) in 2016 where his research focused on the analysis of mass transport mechanisms in oxygen transport membrane porous support layers. His current research involves the product development of PEM fuel cell stacks for automotive applications.



Xuekun Lu is a postdoctoral research associate at electrochemical innovation lab (EIL), University College London. He obtained his PhD in Materials Science at University of Manchester in 2015 and joined UCL in the same year. His research area focuses on the SOFC electrode multi-length scale characterisation and manufacturing optimisation using X-ray tomography and image-based modelling of the mass transport properties in the porous anodes and electrochemical performance.



Francesco Iacoviello is a postdoctoral researcher in the Electrochemical Innovation Lab (EIL), part of the Department of Chemical Engineering at UCL. He gained his PhD from University of Siena (Italy) in 2012 in Mineralogy and Earth Sciences and then moved to University of Sao Paulo (Brazil) where he served as X-Ray diffraction specialist and laboratory manager at the Oceanographic Institute of the same university. Francesco joined EIL in 2015 where his research broadly encompasses the multi-scale X-Ray Computed Tomography characterisation of a different array of materials, from electrochemical devices to geomaterials such as shale gas rock and micrometeorites.



Jason Millichamp is the senior research manager for the Electrochemical Innovation Lab (EIL) based in the Department of Chemical Engineering at UCL. He gained his PhD from UCL in 2013 on Development of a novel high temperature crystal microbalance in-situ sensor for the study of electrode processes in solid oxide fuel cells. His position entails lab and research management of the EIL across its range of electrochemical techniques as well as system design and development.



Dr Paul Shearing is a Reader in Chemical Engineering at UCL. He received his PhD from Imperial College in 2009. He is a pioneer of '4-D Tomography' as recognised by the award of his Royal Academy of Engineering Research Fellowship (2012–16) and has used most of the world's major synchrotron light sources. Paul co-directs the Electrochemical Innovation Lab at UCL and leads the UK STFC Global Challenge Network in Batteries and Electrochemical Devices. In 2014 he was named the Institute of Chemical Engineers, Young Chemical Engineer of the Year and in 2016 the RAEng Young Engineer of the Year.



Dan Brett is Professor of Electrochemical Engineering in the Department of Chemical Engineering at UCL. He gained his PhD from Imperial College London in 2000 on the electrochemistry of self-assembled monolayers. His current research specialises in electrochemical energy conversion and storage, sensors and analytical methods. His work has been recognised by the 2009 DeNora Prize (ISE) and 2011 Baker Medal (ICE). Dan is co-director of the Electrochemical Innovation Lab (EIL), UCL Director of the Centre for Grid Scale Energy Storage, UCL Director of the Centre for Doctoral Training in Fuel Cells and their Fuels and Chairman of Bramble Energy, Ltd.